FRITZ-HABER-INSTITUT
MAX-PLANCK-GESELLSCHAFT

DPG and APS Review 2024

Wahib Aggoune, Lucas Foppa, Kisung Kang, and Sebastian Kokott
April 22, 2024

DPG 2024

MM: Metal and Materials Physics

MM11.6: Uncertainty quantification by direct propagation of shallow ensembles (DPOSE)

Matthias Kellner and Michele Ceriotti

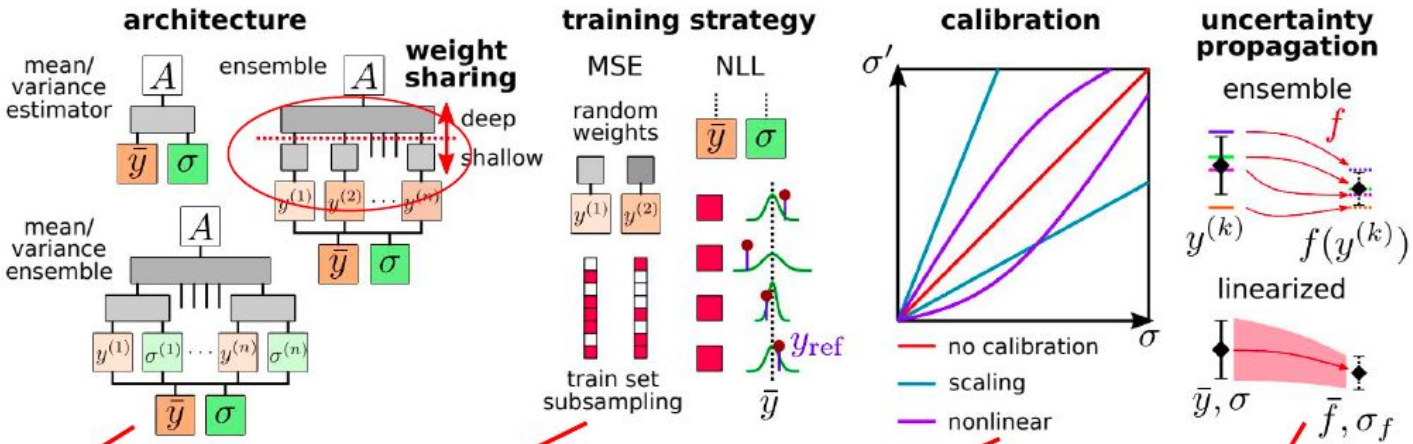

Weight sharing except the last layer

$$\sigma^2_{n_{\mathrm{ens}}}(A) = \frac{1}{n_{\mathrm{ens}} - 1} \sum_{i=1}^{n_{\mathrm{ens}}} [y^{(i)}(A) - \bar{y}(A)]^2$$

Reduced computational overhead

$$\ell^2(A) = (1-\lambda)\frac{1}{2}\left[\log(\sigma_V^2(A)) + \frac{\Delta V(A)^2}{\sigma_V^2(A)}\right] + \frac{\lambda}{3N_A}\sum_{i=1}^{N_A}\sum_{\alpha\in\{x,y,z\}}(\Delta f_{i\alpha})^2,$$

On-the-fly ensemble calibration

$$\sigma_V^2(A) = \frac{1}{n_{\mathrm{ens}} - 1}\sum_k \left[\sum_{A_i \in A} v^{(k)}(A_i) - \bar{V}(A)\right]^2$$

$$\sigma^2_{f_{i\alpha}}(A) = \frac{1}{n_{\mathrm{ens}} - 1}\sum_k \left[\frac{\partial V^{(k)}(A)}{\partial r_{i\alpha}} - \bar{f}_{i\alpha}(A)\right]^2.$$

Propagation on derived quantities

Kellner and Ceriotti, arXiv:2402.16621v1 (2024)

MM11.6: Uncertainty quantification by direct propagation of shallow ensembles (DPOSE)

Matthias Kellner and Michele Ceriotti

Benchmarking of SOAP-BPNN MLIP

Dataset	Model	MAE	RMSE	NLL ↓	RLL ↑	MA ↓
Water	DPOSE(NLL)	218	413	-0.40	59.0	0.04
	MSE	231	369	0.00	33.1	0.09
Li_3PS_4	DPOSE(NLL)	86	213	-1.34	63.7	0.02
	MSE	92	178	-1.12	58.1	0.01
$BaTiO_3$	DPOSE(NLL)	10	21	-2.34	-34.3	0.29
	DPOSE(CRPS)	7	12	-3.41	36.7	0.05
	MSE	7	10	-3.49	31.8	0.06
$QM9(U_0)$	DPOSE(NLL)	26	53	-1.55	2.0	0.18
	DPOSE(CRPS)	26	51	-2.08	41.4	0.04
	MSE	33	54	-1.63	13.2	0.09

Out-of-distribution UQ

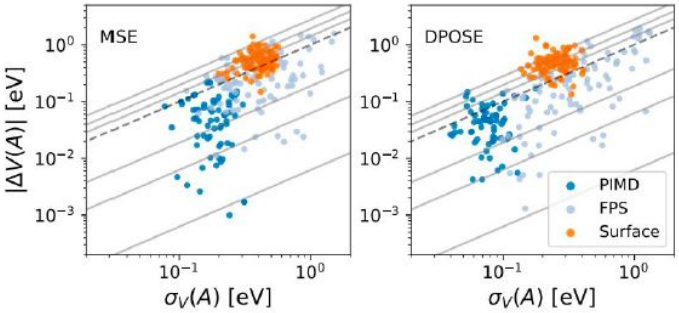

Predicted vs. empirical errors for force components With MLIP-MD on liquid water (500 K)

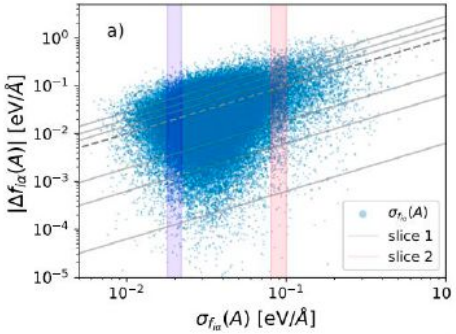

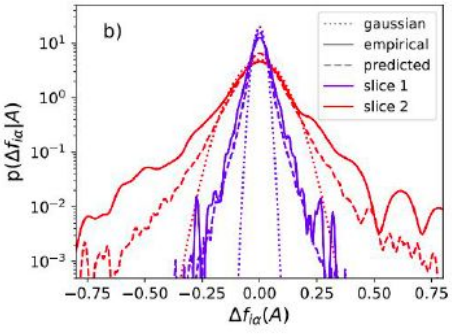

Well-calibrated uncertainty estimates without having explicit force uncertainty term in the loss

Good agreement between predicted and non-Gaussian empirical error distribution

DPOSE features a higher discriminating power between in-distribution and out-of-distribution structures

Kellner and Ceriotti, arXiv:2402.16621v1 (2024)

MM20.6: Experiment-driven atomistic materials modeling:
Combining XPS and MLPs infer the structure of a-COx

Tigany Zarrouk (Miguel Caro's group in Aalto Uni.) *et al.*

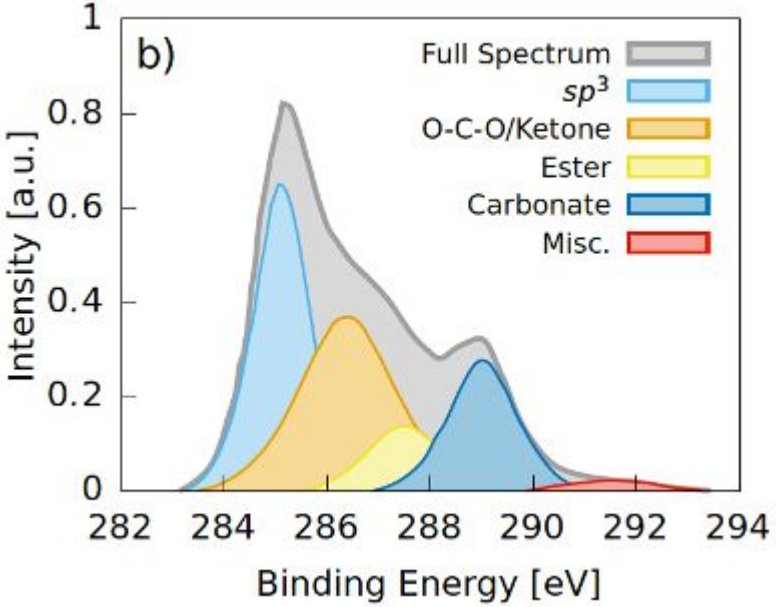

$$\tilde{E} := E_{\text{pot}} + E_{\text{spectra}},$$

1. Generate trial configuration from a randomly chosen MC step type (insertion, removal, move);
2. Evaluate $\tilde{E}$, from Eq. (5);
3. Evaluate the corresponding acceptance criterion, one of Eqs. (6), (7) and (8), and compare to r;
4. Repeat until the target number of MC iterations has been reached.

Reference: https://arxiv.org/pdf/2402.03219.pdf

MM20.6: Experiment-driven atomistic materials modeling:
Combining XPS and MLPs infer the structure of a-COx

Tigany Zarrouk (Miguel Caro's group in Aalto Uni.) *et al.*

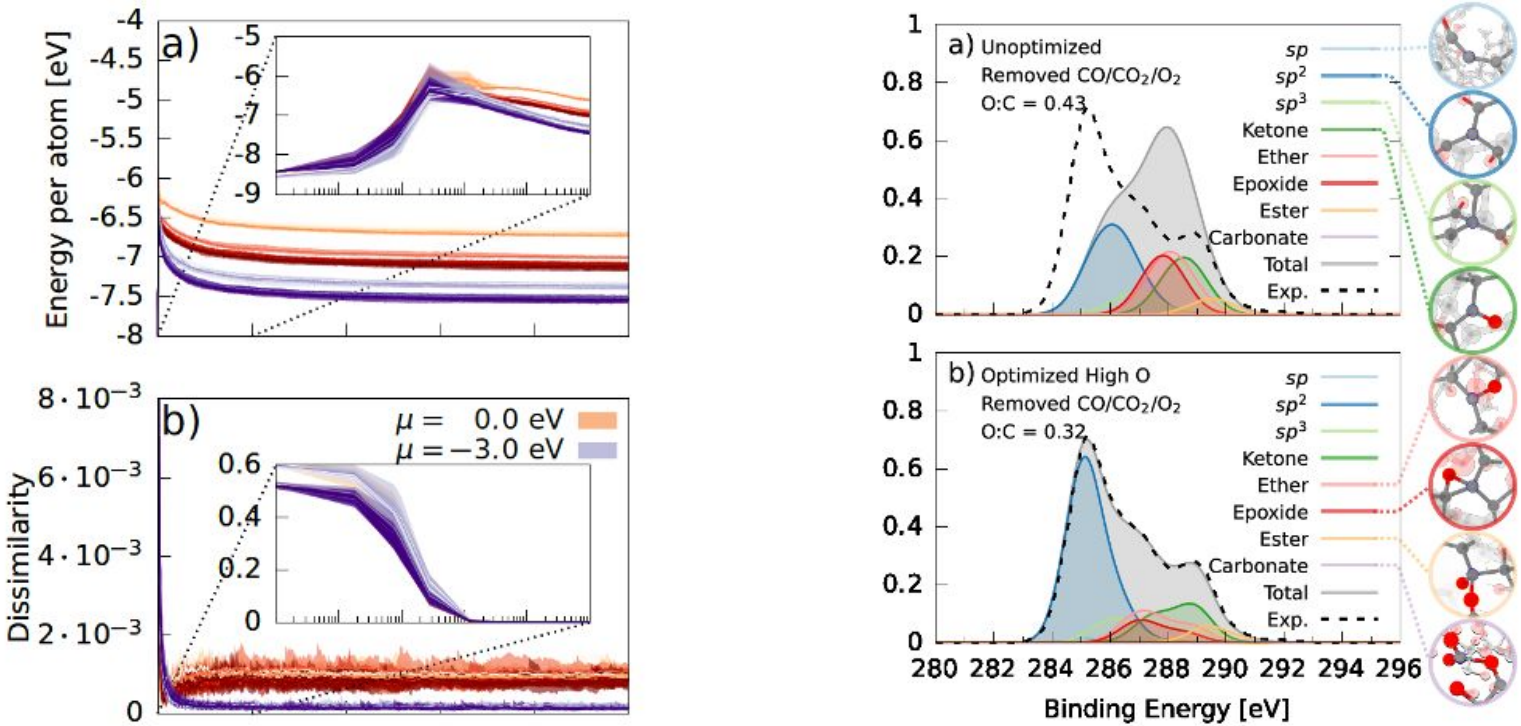

Reference: https://arxiv.org/pdf/2402.03219.pdf

MM25.1: A fuzzy classification framework to identify equivalent atoms in complex materials and molecules King Shun Lai, Sebastian Matera *et al.*

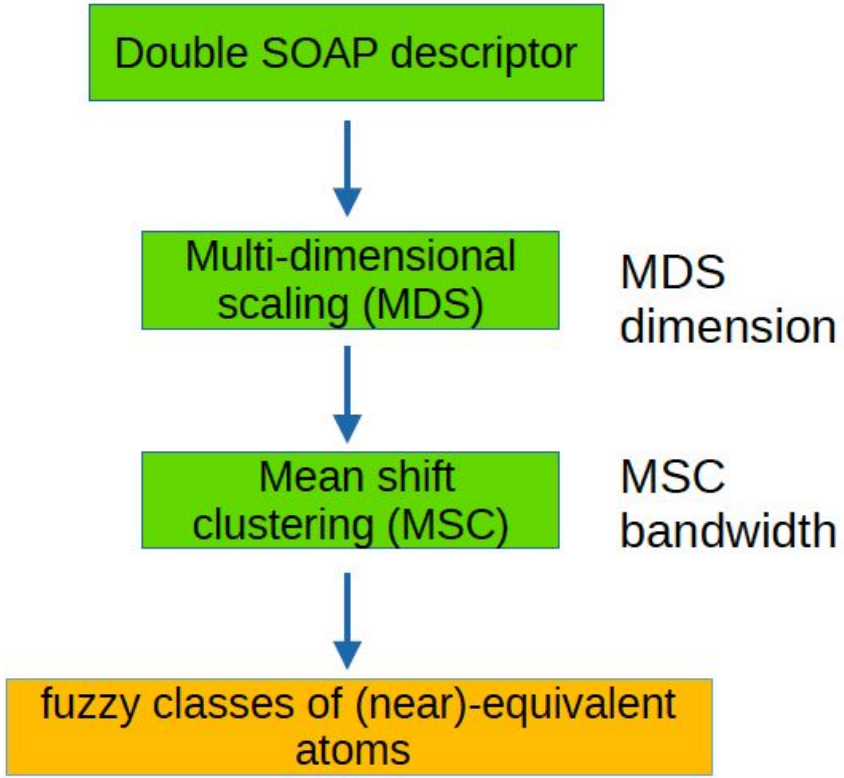

MM25.1: A fuzzy classification framework to identify equivalent atoms in complex materials and molecules

King Shun Lai, Sebastian Matera *et al.*

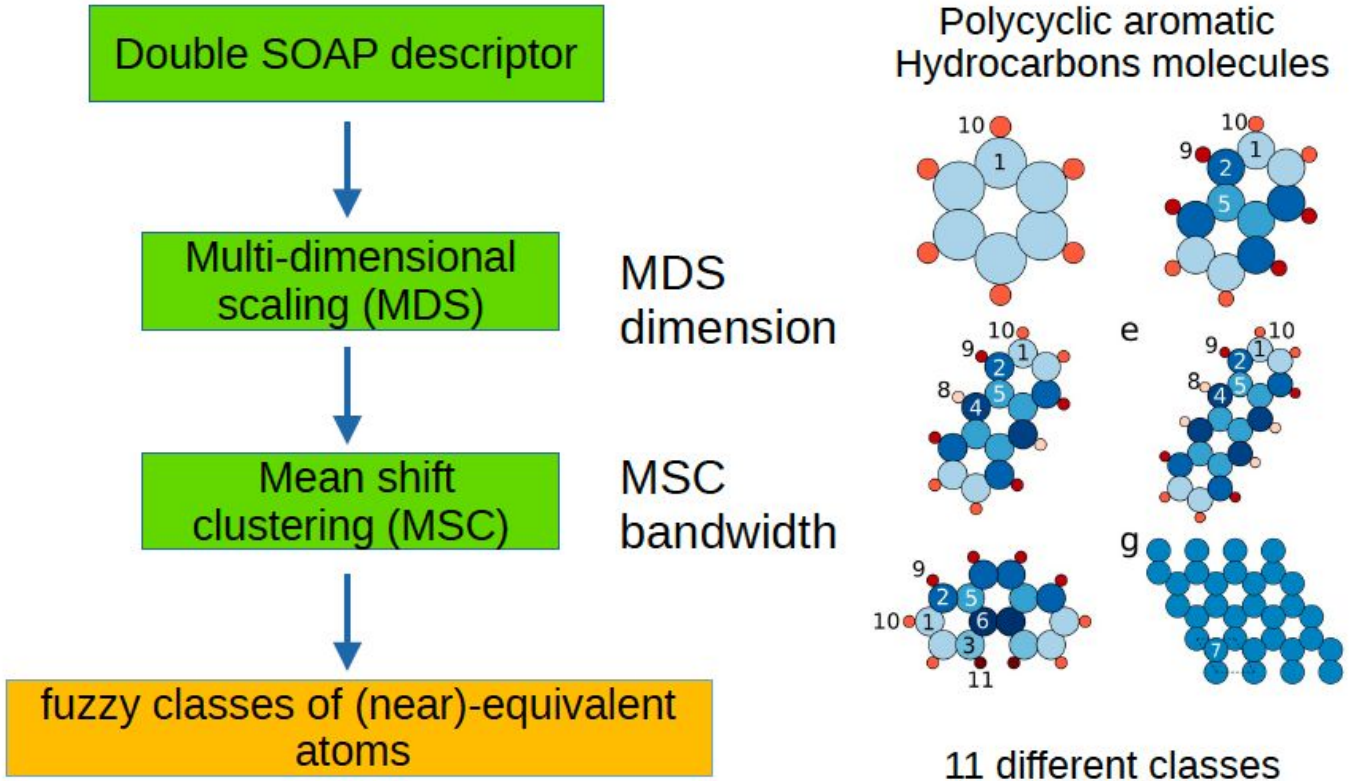

MM25.1: A fuzzy classification framework to identify equivalent atoms in complex materials and molecules

King Shun Lai, Sebastian Matera *et al.*

Double SOAP descriptor

↓

Multi-dimensional scaling (MDS)

MDS dimension

↓

Mean shift clustering (MSC)

MSC bandwidth

↓

fuzzy classes of (near)-equivalent atoms

Polycyclic aromatic Hydrocarbons molecules

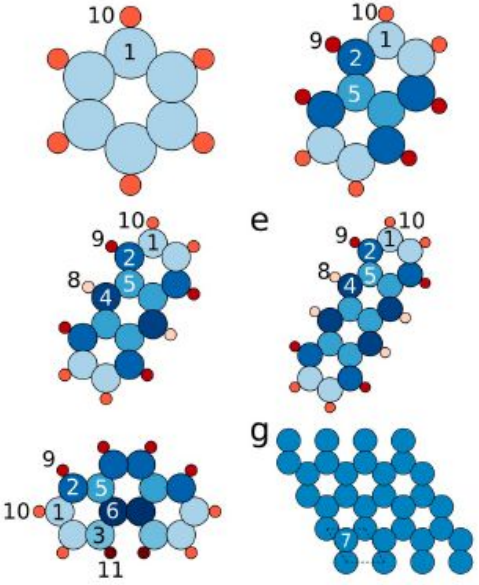

11 different classes

(13x13)Pd(100)

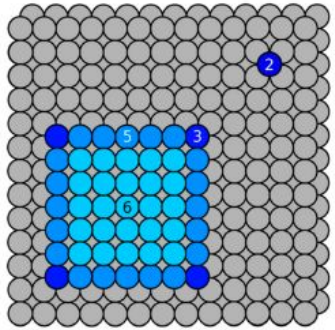

$(14x7\sqrt{3})$Pd(111)

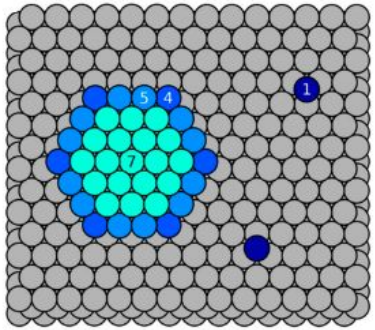

MM62.5: Machine learned interatomic potential for microstructure formation in Ni-rich NiAl systems

Adam Fisher, Peter Brommer *et al.*

Precipitates in nickel-based superalloys form during heat treatment on a time scale inaccessible to direct molecular dynamics simulation, but can be explored using kinetic Monte Carlo (kMC) studies. This requires reliable values for the barrier energies separating distinct atomic configurations. We have previously described a method to find and validate barriers in this system and found that classical potentials such as embedded-atom method (EAM) fail to reproduce the correct ordering of barriers. Modern machine-learned interatomic potentials (MLIPs) have been shown to have an accuracy near that of density functional theory (DFT) at a fraction of the cost. In this work, **we fit an atomic cluster expansion (ACE) MLIP for nickel-rich NiAl systems using ACE hyper-active learning (ACEHAL), training on a series of structures, from cubic unit cells of Ni and Ni3Al to large (>100w atoms) NiAl solid solution cells.** This is complemented by HAL runs on saddle point configurations, which improve the description of energy barriers. The MLIP barriers are then validated and compared to several traditional interatomic potentials.

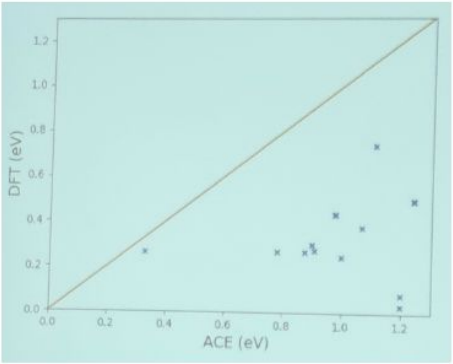

DFT and ACE energy barrier difference

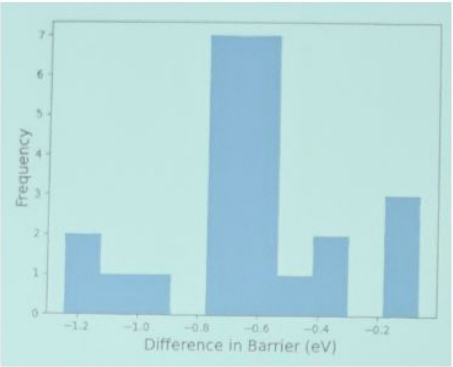

Histogram of the barrier difference

O: Surface Physics

O1: (Surface-)science-driven machine learning

Johannes T. Margraf

This talk discusses research towards the establishment of a science-driven approach to machine learning (ML) for surface science and chemistry [1]. In many fields, ML is a fundamentally data-driven endeavour, meaning that specific databases and benchmark problems (i.e. big data) are at the center of methodological development. While this has certainly led to tremendous advances in recent years (e.g. in image generation and natural language processing), the full diversity and complexity of surface chemistry cannot be adequately represented by static predefined databases. We therefore aim to build accurate data-efficient models which do not require enormous reference datasets for training. This way, our methods can be applied to a wide range of problems of scientific interest and not just to those for which big data happens to be available. To this end, we explicitly incorporate chemical and physical information into the ML models [2] and integrate the data generation or selection process with the model training [3]. Several examples of this in the context of the atomistic simulation of catalytic processes on surfaces will be discussed.

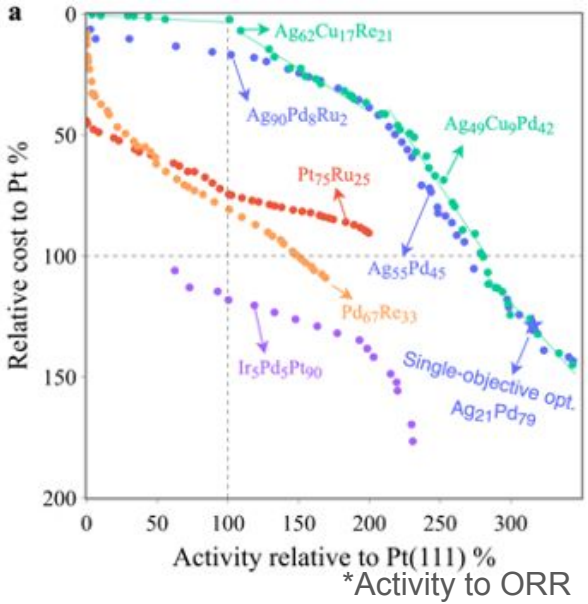

*Activity to ORR

[1] J.T. Margraf, Angew. Chemie, 62, e202219170 (2023). [2] K. Chen et al. Chem. Sci., 14, 4913-4922 (2023).
[3] H. Jung et al. NPJ Comput. Mater., 9, 114 (2023).

O10.5: Multi-channel Dyson equation: coupling many-body Green's functions

Arjan Berger

We present the multichannel Dyson equation that combines two or more many-body Green's functions to describe the electronic structure of materials. In this work we use it to model photoemission spectra by coupling the one-body Green's function with the three-body Green's function. We demonstrate that, unlike methods using only the one-body Green's function, our approach puts the description of quasi-particles and satellites on an equal footing. We propose a multichannel self-energy that is static and only contains the bare Coulomb interaction, making frequency convolutions and self-consistency unnecessary. Despite its simplicity, we demonstrate with a diagrammatic analysis that the physics it describes is extremely rich. Finally, we present a framework based on an effective Hamiltonian that can be solved for any many-body system using standard numerical tools.

$$G_3(\omega) = G_{03}(\omega) + G_{03}(\omega)\Sigma_3(\omega)G_3(\omega),$$

Frequency independent
Only uses bare Coulomb

$$G_{03}(\omega) = \begin{pmatrix} G_{01}(\omega) & 0 \\ 0 & G_{03}^{3p}(\omega) \end{pmatrix}, \quad \Sigma_3 = \begin{pmatrix} \Sigma^{1p} & \Sigma^{c} \\ \tilde{\Sigma}^{c} & \Sigma^{3p} \end{pmatrix}$$

Third iteration:

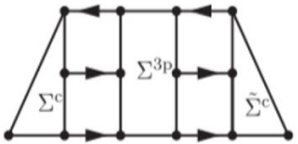

includes

(ring diagram in GW/RPA)

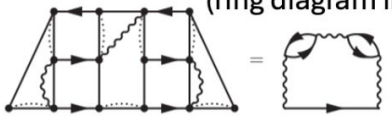

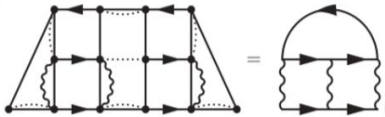

(beyond GW/RPA)

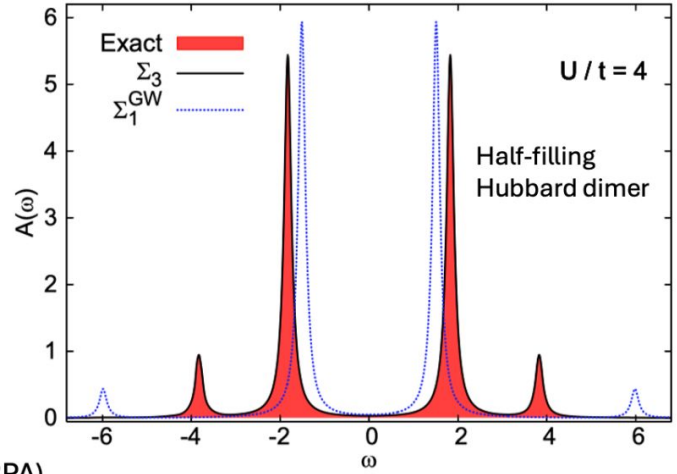

O42.5: Quasiparticle Self-Consistent *GW* Study of Simple Metals

Christoph Friedrich *et al.*

… We show that, while DFT overestimates the bandwidth of most of the materials, the ***GW* quasiparticle renormalization corrects the bandwidths in the right direction**, but a full self-consistent calculation is needed to consistently achieve good agreement with photoemission data. The results mainly confirm the common belief that simple metals can be regarded as nearly free electron gases with weak electronic correlation.

	Li	Be		Na	Mg			K	Ca
LDA	3.46	11.02	4.26	3.29	6.87	1.62	1.28	2.16	3.98
LDA [1]	3.46	11.03	4.28	3.30	6.89	1.65	1.31	2.15	3.98
G_0W_0	3.22	11.31	4.41	3.04	6.58	1.63	1.24	1.95	3.60
G_0W_0 [1]	3.39	11.37	4.48	3.15	6.66	1.68	1.29	2.00	3.79
QSGW	3.10	11.14	4.36	2.90	6.52	1.64	1.21	1.88	3.60
QSGW [2]				3.00					
LQSGW [3]				3.16				2.07	
eDMFT [1]	2.60	10.12	4.41	2.84	6.18	1.85	0.82	1.42	3.24
exp	3.0 [4]	11.1	4.8 [6]	2.65 [7]	6.15	1.7	0.9 [9]	1.6 [11]	3.3 [12]
		11.15 [5]		2.78 [8]	6.89	1.79	1.23 [10]		3.6 [13]

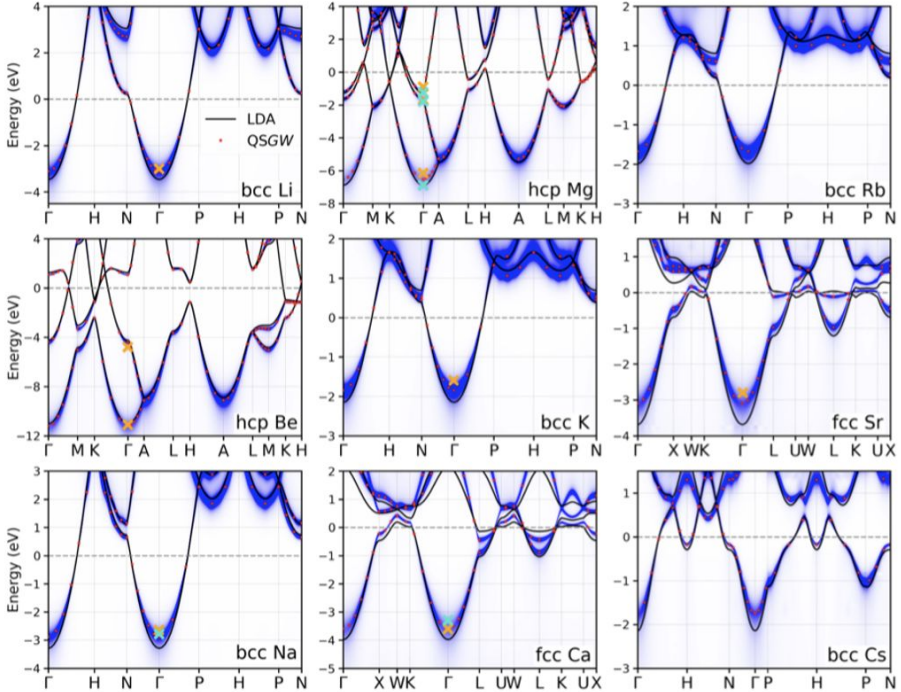

O50.4: Cu Oxide Nanoparticles for Virus Inactivation

Daniel Silvan Dolling *et al.*

Copper and its oxides are well known for their antiviral and antibacterial properties, more recently including the inactivation of SARS-CoV-2 [1, 2, 3]. The combination of Cu oxides with TiO_2 has attracted interest due to the photocatalytic activity of the combined system.

For the photocatalytic activity, the specific oxidation state of Cu is paramount, as the oxidation states offer different pathways for visible light activity. Up to now, most research regarding virus inactivation has focused on powder systems. Here, we investigate the effects of different Cu nanoparticle sizes and coverages on single crystalline TiO_2(110) surface by X-ray photoelectron spectroscopy(XPS). Moreover, as the oxide state is playing a major role in the (photo-)activity, we investigate the in-situ oxidation of Cu nanoparticles via XRD, XPS and SEM.

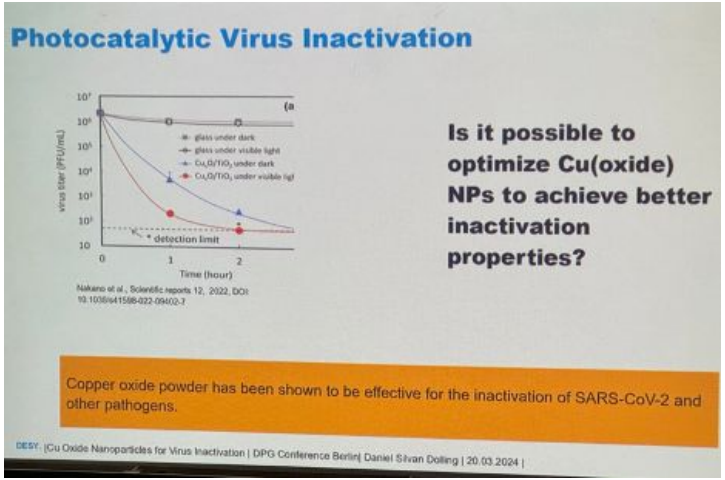

[1] M. Hosseini et al., Scientific Reports 12 (2021), 5919-5928. [2] A. Purniawan et al., Scientific Reports 12 (2022).
[3] M. Liu et al., J. Mater. Chem. A 3 (2015), 17312-17319.

O82.6: Electronic excited states from physically constrained machine learning

Divya Suman and Michele Ceriotti

Indirect learning of symmetry-adapted of pseudo-Hamiltonian

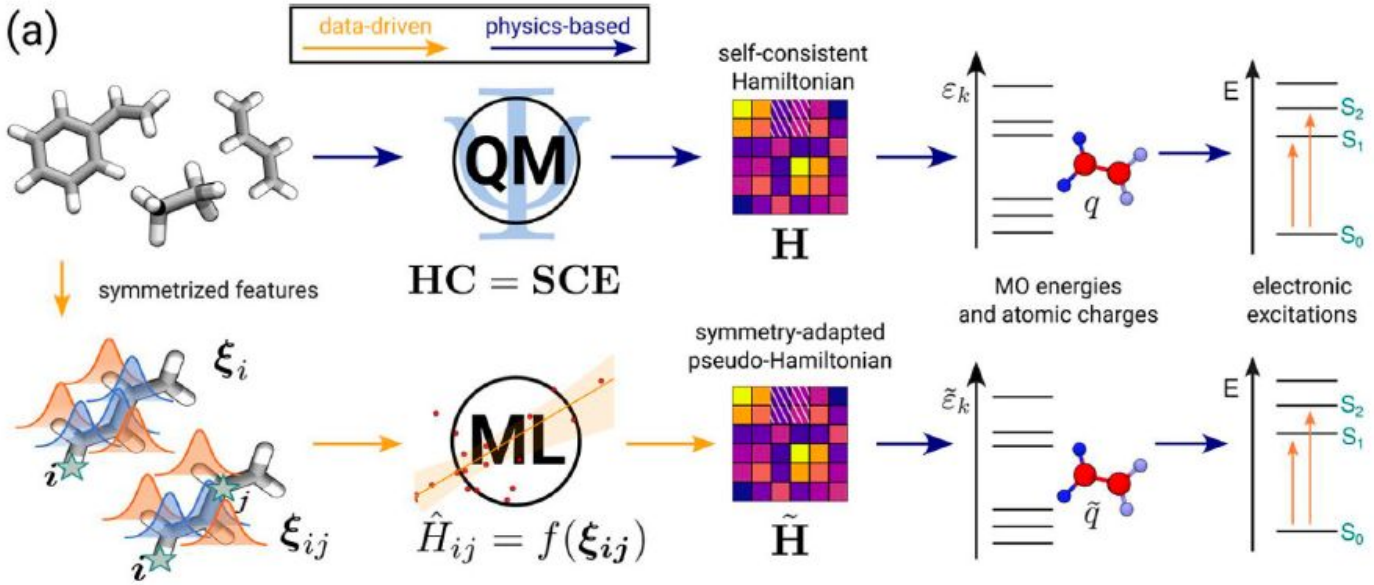

Best training protocol

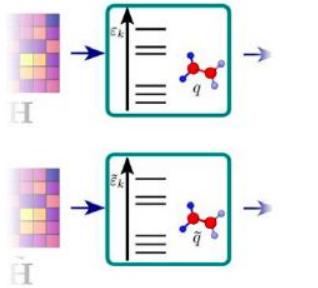

Combining multiple targets leads to more accurate and generaziable model for both eigenvalues and atomic charges compared to direct Hamiltonian learning under minimal basis

Cignoni *et al., ACS Cent. Sci.* (2024)

O82.6: Electronic excited states from physically constrained machine learning

Divya Suman and Michele Ceriotti

Large basis sets

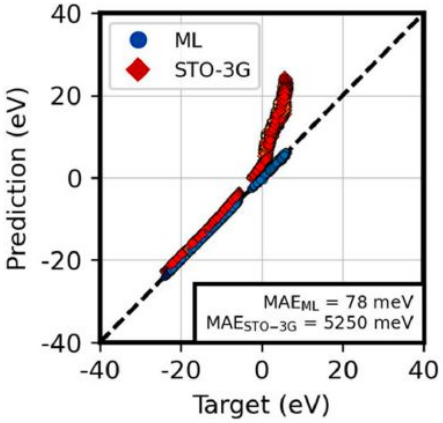

Electronic excitations

Target: sTDA B3LYP/def2-TZVP
Prediction: ML + sTDA

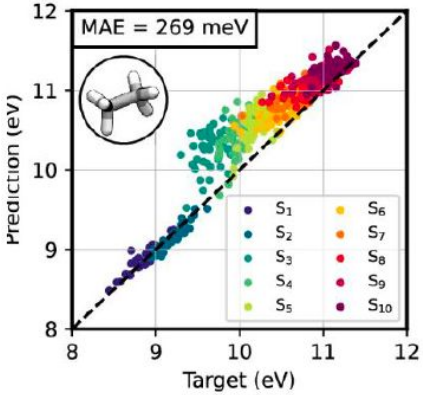

Generalization

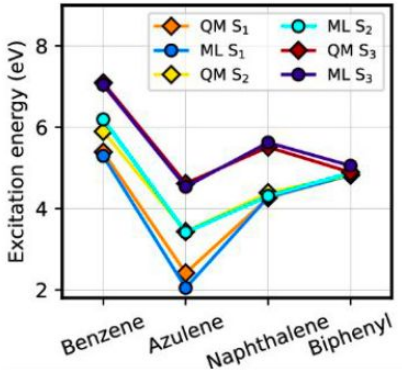

Vibrational Spectra (Anthracene)

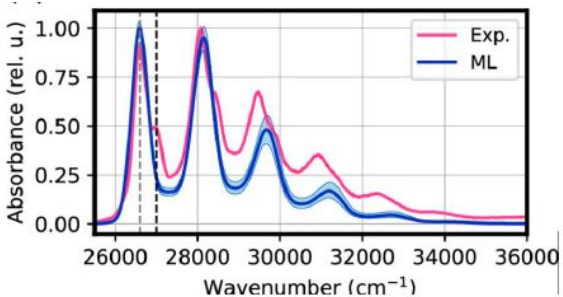

Excellent transferability for evaluation of derived electronic properties and making predictions for larger, more complex compounds

Take home message: "*Reproducing the mathematical structure of the quantum mechanical approximations is more effective than explicitly targeting the value of approximate electronic-structure quantities*"

Cignoni *et al., ACS Cent. Sci.* (2024)

O96.3: The mechanism of electrochemical CO_2 reduction to post Co and C_{2+} products over single atom catalysts

Michael Busch *et al.*

Electrochemical reduction of CO_2 to CO or post CO products is of central importance for energy storage and conversion. A promising class of catalysts for CO_2 reduction are single atom catalysts (SACs) which consist of a single metal atom embedded into graphene. These materials are generally believed to only form C_1 compounds. However, recent experiments indicate, that methane together with minor amounts of products with 2 or more carbon atoms are formed over Fe phthalocyanine complexes, which are structurally similar to classical SACs [1].

In this contribution we will explore the reaction routes from CO_2 to methane and C_{2+} compounds using density functional theory (DFT) computations [2]. Our results indicate, that the selectivity between different products mainly depends on activation barriers and is strongly influenced by the CO and proton concentration close to the electrode.

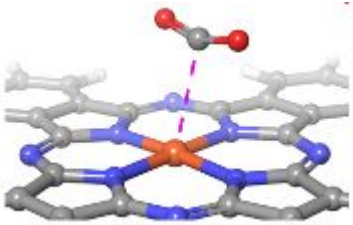

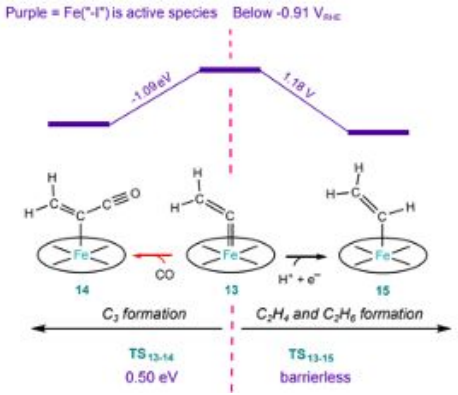

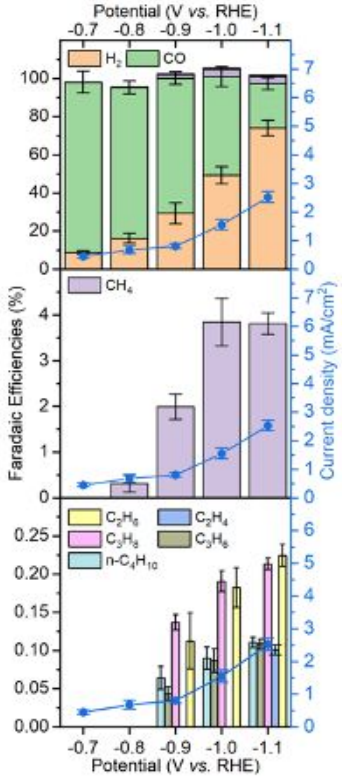

[1] S.-T. Dong, C. Xu, B. Lassalle-Kaiser *Chem. Sci.* 14 (2023) 550.
[2] R. Khakpour, K. Farshadfar, M. Busch et al. *submitted*.

TT: Low Temperature Physics

TT 2.8: Machine determination of a phase diagram with and without deep learning

Burak Çivitioğlu *et al.*

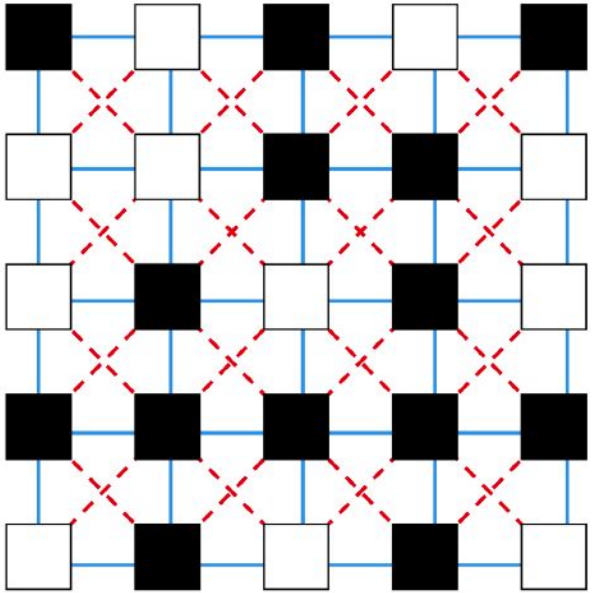

J1-J2 Ising model on a 5×5 square lattice

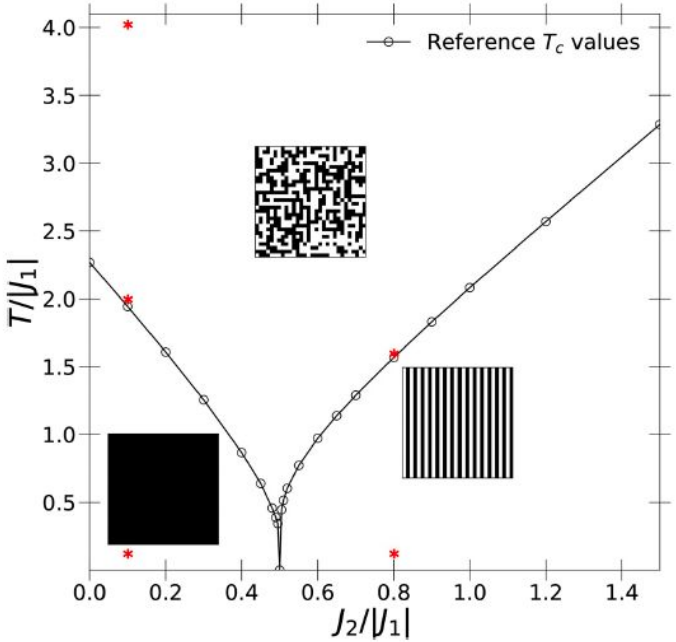

Phase diagram of the J1-J2 Ising model on the periodic square lattice

$$H_{J_1 J_2} = -J_1 \sum_{\langle i,j \rangle} s_i s_j + J_2 \sum_{\langle\langle i,j \rangle\rangle} s_i s_j$$

TT 2.8: Machine determination of a phase diagram with and without deep learning

Burak Çivitioğlu *et al.*

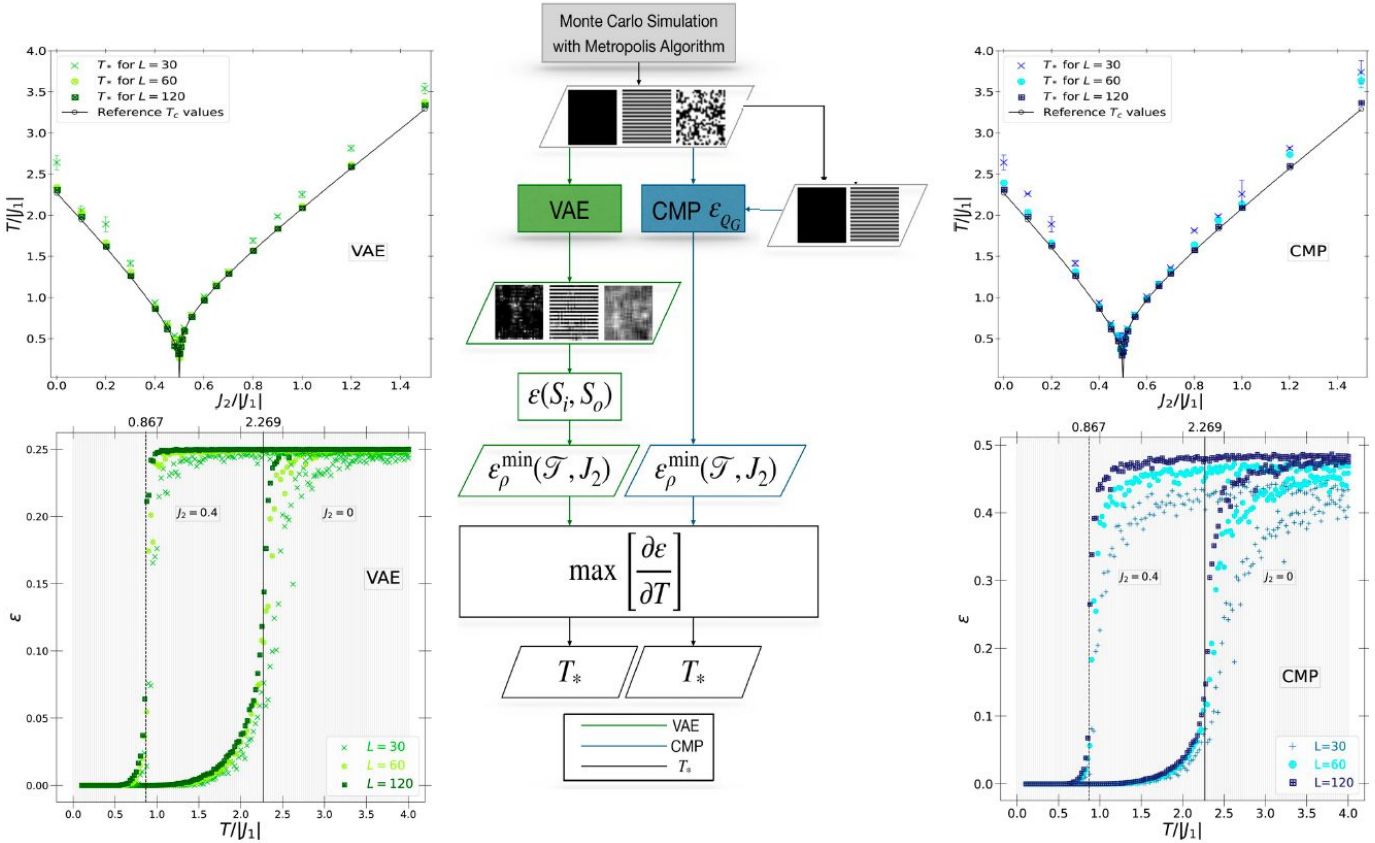

HL: Semiconductor Physics

HL38.5: Growth, catalysis, and faceting of α-Ga_2O_3 and α-$(In_xGa_{1-x})_2O_3$ on m-plane α-Al_2O_3 by molecular beam epitaxy

Martin S. Williams, Patrick Vogt *et al.*

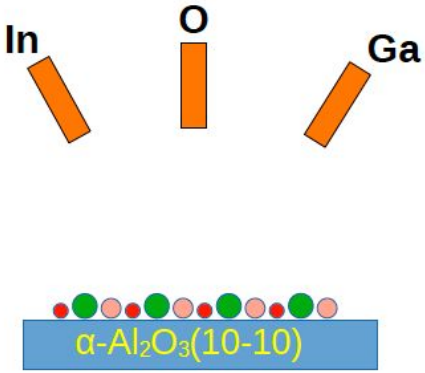

M. Williams et al., APL Mater. 12, 011120 (2024)

HL38.5: Growth, catalysis, and faceting of α-Ga_2O_3 and α-$(In_xGa_{1-x})_2O_3$ on m-plane α-Al_2O_3 by molecular beam epitaxy

Martin S. Williams, Patrick Vogt *et al.*

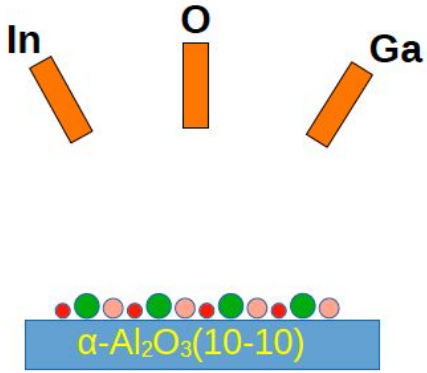

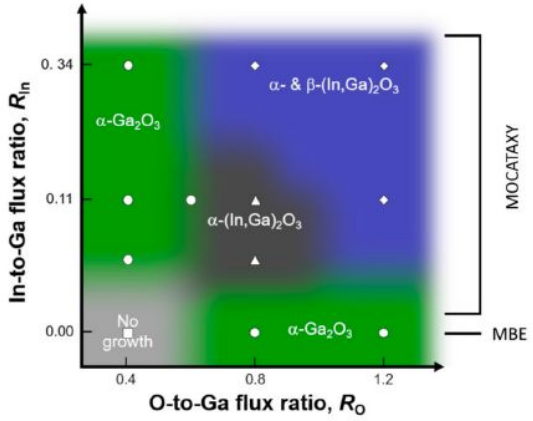

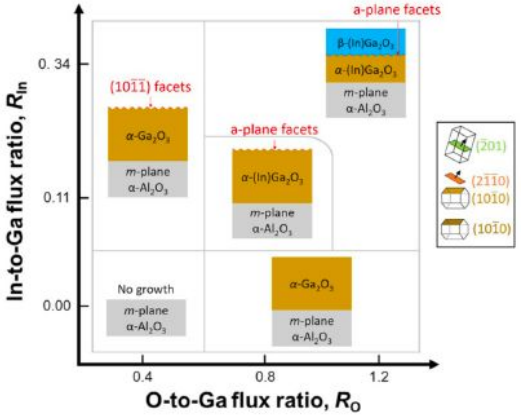

- Formation of α-$(In_xGa_{1-x})_2O_3$, □-$(In_xGa_{1-x})_2O_3$, α-Ga_2O_3
- R_{Me}>2 In acts as catalysts and expand the Ga_2O_3 growth windows
- R_{Me}<2 In incorporate in the layer

M. Williams et al., APL Mater. 12, 011120 (2024)

HL38.5: Growth, catalysis, and faceting of α-Ga_2O_3 and α-$(In_xGa_{1-x})_2O_3$ on m-plane α-Al_2O_3 by molecular beam epitaxy

Martin S. Williams, Patrick Vogt *et al.*

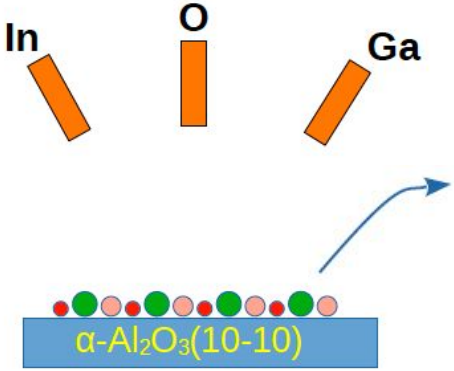

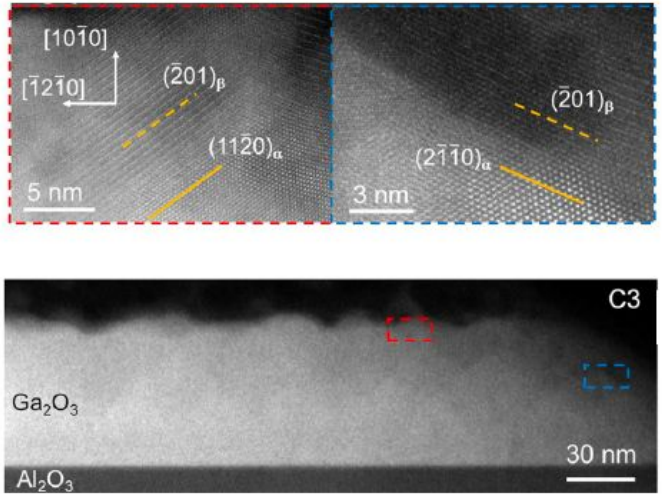

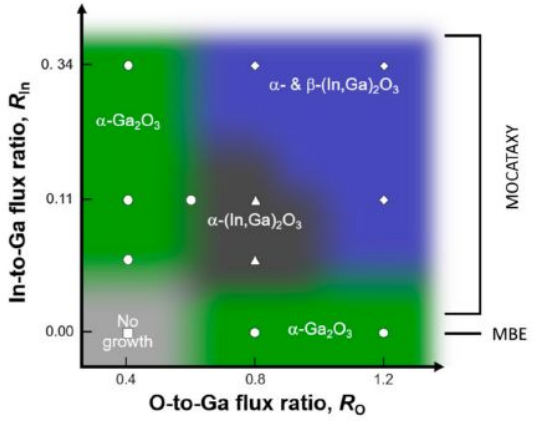

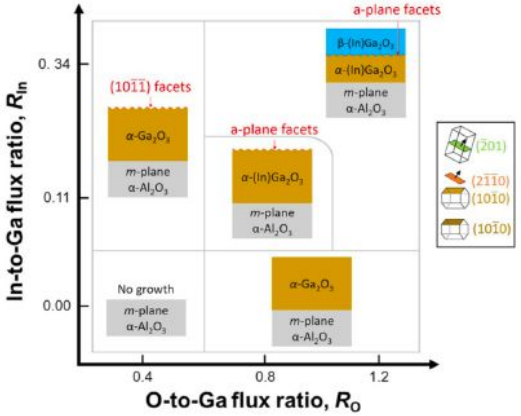

- Formation of α-$(In_xGa_{1-x})_2O_3$, □-$(In_xGa_{1-x})_2O_3$, α-Ga_2O_3
- R_{Me}>2 In acts as catalysts and expand the Ga_2O_3 growth windows
- R_{Me}<2 In incorporate in the layer

M. Williams et al., APL Mater. 12, 011120 (2024)

SYES:
Symposium Advances in Ab-Initio Electronic Structure Theory of Time-Dependent and Non-Equilibrium Phenomena

SYES 1.2: Probing the transport of the interacting electron-phonon system self-consistently and ab initio

Nakib Protik

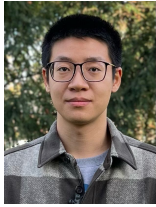

elphbolt

https://github.com/nakib/elphbolt

∇T field:

$$\text{e: } \mathbf{I}_{m\mathbf{k}} = \mathbf{I}^0_{m\mathbf{k}} + \Delta\mathbf{I}^{\mathrm{S}}_{m\mathbf{k}}[\mathbf{I}_{m\mathbf{k}}] + \Delta\mathbf{I}^{\mathrm{D}}_{m\mathbf{k}}[\mathbf{F}_{s\mathbf{q}}]$$

$$\text{ph: } \mathbf{F}_{s\mathbf{q}} = \mathbf{F}^0_{s\mathbf{q}} + \Delta\mathbf{F}^{\mathrm{S}}_{s\mathbf{q}}[\mathbf{F}_{s\mathbf{q}}] + \Delta\mathbf{F}^{\mathrm{D}}_{s\mathbf{q}}[\mathbf{I}_{m\mathbf{k}}]$$

$\mathbf{E}$ field:

$$\text{e: } \mathbf{J}_{m\mathbf{k}} = \mathbf{J}^0_{m\mathbf{k}} + \Delta\mathbf{J}^{\mathrm{S}}_{m\mathbf{k}}[\mathbf{J}_{m\mathbf{k}}] + \Delta\mathbf{J}^{\mathrm{D}}_{m\mathbf{k}}[\mathbf{G}_{s\mathbf{q}}]$$

$$\text{ph: } \mathbf{G}_{s\mathbf{q}} = \cancelto{0}{\mathbf{G}^0_{s\mathbf{q}}} + \Delta\mathbf{G}^{\mathrm{S}}_{s\mathbf{q}}[\mathbf{G}_{s\mathbf{q}}] + \Delta\mathbf{G}^{\mathrm{D}}_{s\mathbf{q}}[\mathbf{J}_{m\mathbf{k}}].$$

In the materials where phonons and the charge carriers coexist and interact with each other, the transport of one system induces the transport of the other. This is known as the mutual electron-phonon drag. In order to capture the dragful charge, heat, and thermoelectric transport in such materials, the kinetic equations of both types of quasiparticles have to be solved self-consistently. While the formal structure of the coupled kinetic equations has been known since 1930 [1], it is only recently that a fully ab initio, coupled electron-phonon Boltzmann transport formalism, called elphbolt [2], has been developed. This has opened the avenue for the parameters-free and in silico probing of the dragful transport.

[1] Peierls, R. Ann. Phys. 396, 121-148 (1930).
[2] Protik, et al. npj Comput Mater 8, 28 (2022).

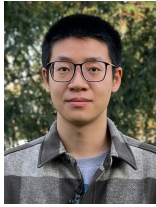

SYES 1.2: Probing the transport of the interacting electron-phonon system self-consistently and ab initio

Nakib Protik

ph-ph scattering:

$$\begin{Bmatrix} \mathbf{F}^0_{s\mathbf{q}} \\ \mathbf{G}^0_{s\mathbf{q}} \end{Bmatrix} = \begin{Bmatrix} \hbar\omega_{s\mathbf{q}}/T \\ 0 \end{Bmatrix} \frac{\mathbf{v}_{s\mathbf{q}}}{W^{\mathrm{RTA}}_{s\mathbf{q}}},$$

phonon self term:

$$\begin{Bmatrix} \Delta\mathbf{F}^{\mathrm{S}}_{s\mathbf{q}} \\ \Delta\mathbf{G}^{\mathrm{S}}_{s\mathbf{q}} \end{Bmatrix} = \frac{1}{n^0_{s\mathbf{q}}(1+n^0_{s\mathbf{q}})} \frac{1}{W^{\mathrm{RTA}}_{s\mathbf{q}}} \times \sum_{s'\mathbf{q}'s''\mathbf{q}''} \left[W^{+}_{s\mathbf{q}s'\mathbf{q}'|s''\mathbf{q}''} \begin{Bmatrix} \mathbf{F}_{s''\mathbf{q}''} - \mathbf{F}_{s'\mathbf{q}'} \\ \mathbf{G}_{s''\mathbf{q}''} - \mathbf{G}_{s'\mathbf{q}'} \end{Bmatrix} + \frac{1}{2} W^{-}_{s\mathbf{q}s'\mathbf{q}'|s''\mathbf{q}''} \begin{Bmatrix} \mathbf{F}_{s''\mathbf{q}''} + \mathbf{F}_{s'\mathbf{q}'} \\ \mathbf{G}_{s''\mathbf{q}''} + \mathbf{G}_{s'\mathbf{q}'} \end{Bmatrix} \right]$$

ph-e drag term:

$$\begin{Bmatrix} \Delta\mathbf{F}^{\mathrm{D}}_{s\mathbf{q}} \\ \Delta\mathbf{G}^{\mathrm{D}}_{s\mathbf{q}} \end{Bmatrix} = \frac{d_s}{n^0_{s\mathbf{q}}(1+n^0_{s\mathbf{q}})} \frac{1}{W^{\mathrm{RTA}}_{s\mathbf{q}}} \sum_{mn\mathbf{k}} Y_{s\mathbf{q}|m\mathbf{k}n\mathbf{k}'} \begin{Bmatrix} \mathbf{I}_{n\mathbf{k}'} - \mathbf{I}_{m\mathbf{k}} \\ \mathbf{J}_{n\mathbf{k}'} - \mathbf{J}_{m\mathbf{k}} \end{Bmatrix}.$$

SYES 1.2: Probing the transport of the interacting electron-phonon system self-consistently and ab initio Nakib Protik

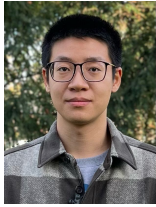

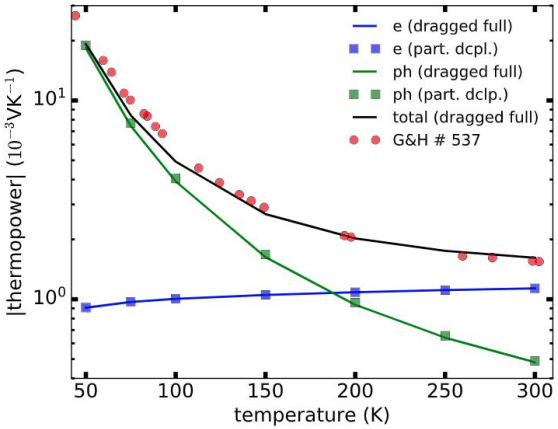

Fig. 2 Temperature dependence of the thermopower of silicon for an *n*-type carrier concentration of 2.75×10^{14} cm^{-3}. The red circles are measurements (sample 537, concentration 2.8×10^{14} cm^{-3}) by Geballe and Hull[15].

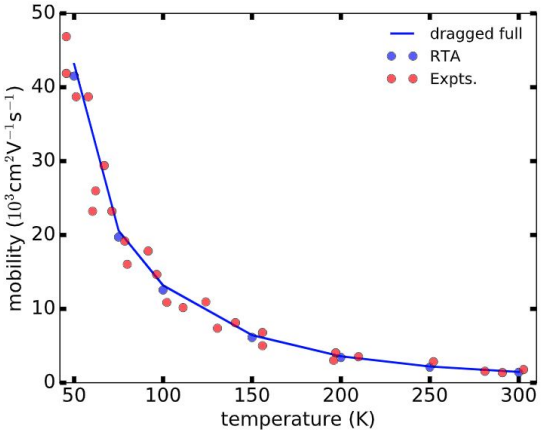

Fig. 4 Temperature dependence of the mobility of silicon for an *n*-type carrier concentration of 2.75×10^{14} cm^{-3}. The red circles are measurements on various different samples with carrier concentrations ranging from 3.5×10^{13} to 1.4×10^{14} cm^{-3}[52].

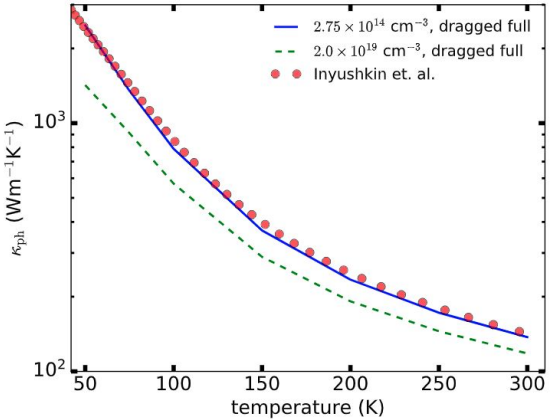

Fig. 6 Temperature dependence of the phonon thermal conductivity of silicon for *n*-type carrier concentrations of 2.75×10^{14} and 2×10^{19} cm^{-3}. The red circles are measurements on high purity samples with natural isotopic mix[57].

Drag term plays important role in Seebeck coefficient, and less important role in mobility and phonon thermal conductivity, especially at high temperatures.

APS 2024

F18.00009 Uncovering interpretable low-dimensional geometric structures in gene expression using curvature regularized variational autoencoders Jason Kim *et al.*

Meso-scale structure in Dimension reduction

Dimension reduction in ML.

PCA - linear model -> have meso-scale structure

t-SNE
UMAP - two popular nonlinear model
-> no meso-scale structure

Γ-VAE (this talk) - nonlinear model with Curvature regularization
Normal VAE + curvature regularization

UMAP cluster close in UMAP doesn't guarantee similar

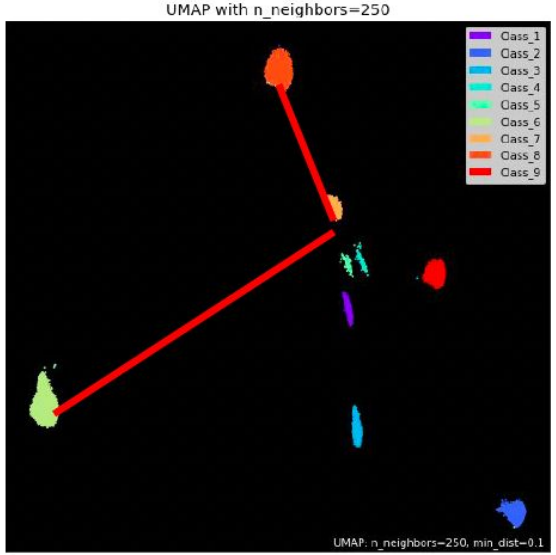

https://www.kaggle.com/code/bextuychiev/beautiful-umap-tutorial-on-100-dimensional-data

Kim, J. Z., Perrin-Gilbert, N., Narmanli, E., Klein, P., Myers, C. R., Cohen, I., ... & Sethna, J. P. (2024). $\Gamma $-VAE: Curvature regularized variational autoencoders for uncovering emergent low dimensional geometric structure in high dimensional data. arXiv preprint arXiv:2403.01078.

F18.00009 Uncovering interpretable low-dimensional geometric structures in gene expression using curvature regularized variational autoencoders Jason Kim *et al.*

Meso-scale structure (Long-range covariance)

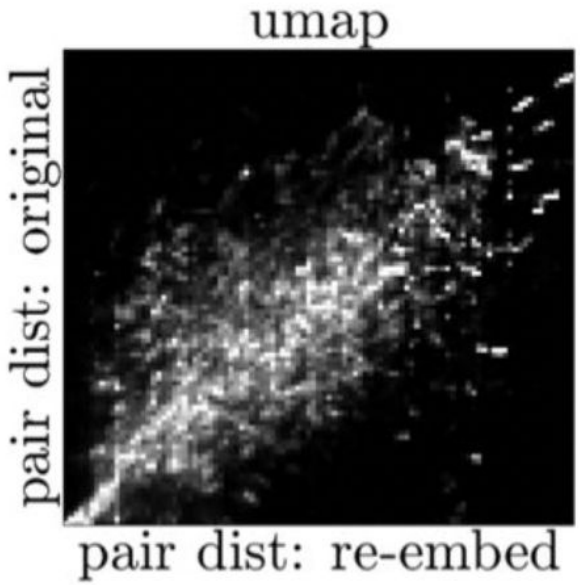

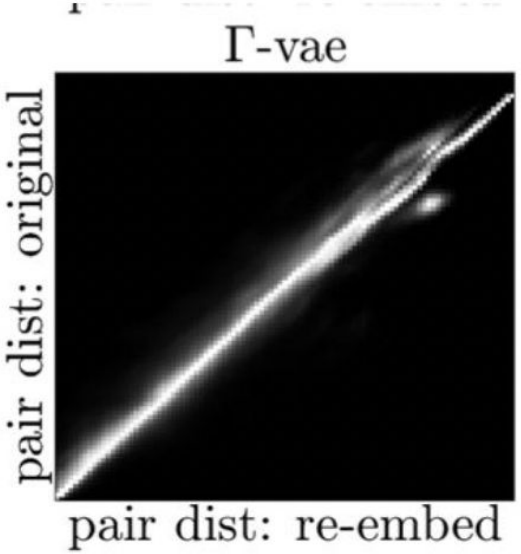

curvature regularization for the manifold.

Kim, J. Z., Perrin-Gilbert, N., Narmanli, E., Klein, P., Myers, C. R., Cohen, I., ... & Sethna, J. P. (2024). $\Gamma $-VAE: Curvature regularized variational autoencoders for uncovering emergent low dimensional geometric structure in high dimensional data. arXiv preprint arXiv:2403.01078.

F18.00009 Uncovering interpretable low-dimensional geometric structures in gene expression using curvature regularized variational autoencoders Jason Kim *et al.*

A “global” embedding of all kinds of cells by gene expression

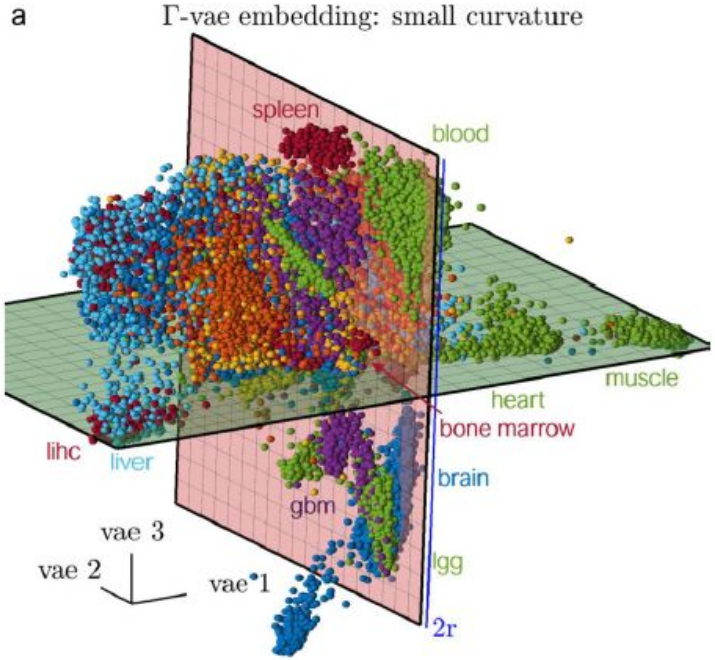

A 3D map for the cells

N62.00006 Materials Discovery Using Simulations and Deep Learning

Uwe Bergmann

Toward **Universal Force Field**

~48000 known stable structure => 2.2 million stable structure (based on convex hull)

Nequip model for bulk solids with all elements

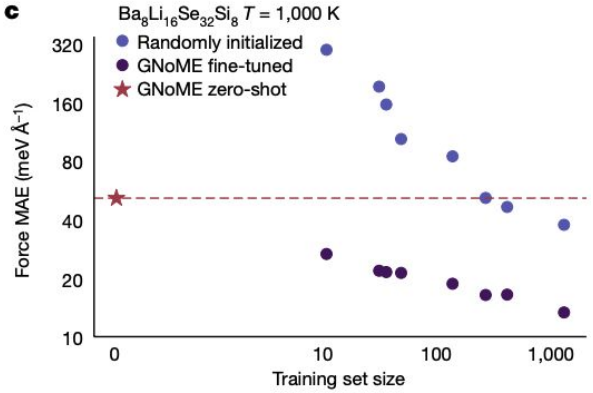

We also use SiLU for the gated, equivariant nonlinearities[68]. We embed the chemical species using a 94-element one-hot encoding and use a self-connection, as proposed in ref. 30. For internal normalization, we

Pretrained on atomic relaxation data (>10^8 data points). Works fine for molecular dynamics. Pretrained model seems to be pretty reliable with error similar to randomly initialized model trained on ~1000 data points

A. Merchant *et al.*, *Nature* **624**, 80 (2023).

N62.00006 Materials Discovery Using Simulations and Deep Learning

Uwe Bergmann

Significantly augment materials data through ionic substitution and symmetry-aware partial substitutions.
→ 10^9 Candidate materials (Large enough to observe the Emergence in materials science)

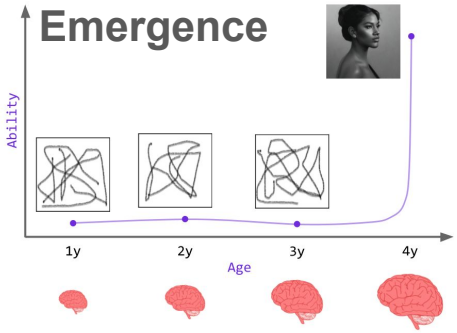

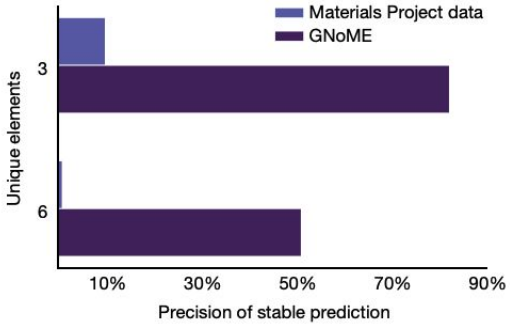

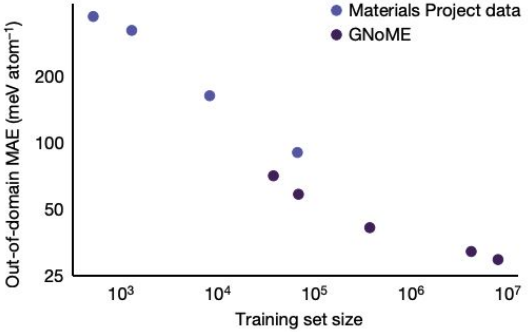

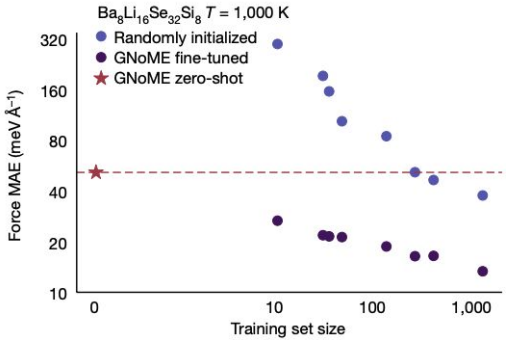

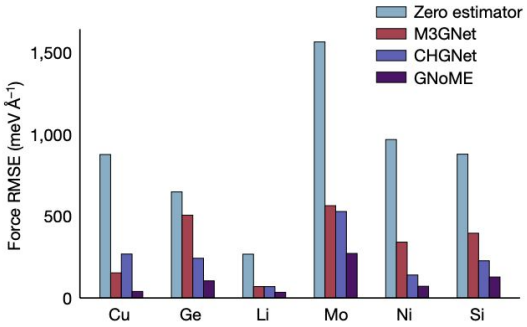

A. Merchant *et al.*, *Nature* **624**, 80 (2023).

N62.00006 Materials Discovery Using Simulations and Deep Learning

Uwe Bergmann

	F1 ↑	DAF ↑	Prec ↑	Acc ↑	TPR ↑	TNR ↑	MAE ↓	RMSE ↓	R^2 ↑	Training Size	Model Params	Model Type	Targets
GNoME	0.83	5.52	0.84	0.95	0.81	0.97	0.04	0.09	0.79	89.0M (6.0M)	16.2M	UIP	EF
MACE	0.67	3.78	0.58	0.88	0.80	0.89	0.06	0.10	0.70	1.6M (145.9K)	4.7M	UIP	EFS
CHGNet	0.61	3.36	0.51	0.85	0.76	0.87	0.06	0.10	0.69	1.6M (145.9K)	412.5K	UIP	EFSM
M3GNet	0.57	2.88	0.44	0.81	0.80	0.81	0.07	0.12	0.58	188.3K (62.8K)	227.5K	UIP	EFS
ALIGNN	0.57	3.21	0.49	0.84	0.67	0.87	0.09	0.15	0.30	154.7K	4.0M	GNN	E
MEGNet	0.51	2.96	0.45	0.83	0.58	0.87	0.13	0.21	-0.25	133.4K	167.8K	GNN	E
CGCNN	0.51	2.85	0.44	0.82	0.60	0.86	0.14	0.23	-0.60	154.7K	128.4K	GNN	E
CGCNN+P	0.50	2.56	0.39	0.79	0.69	0.80	0.11	0.18	0.02	154.7K	128.4K	GNN	E
Wrenformer	0.47	2.26	0.34	0.74	0.72	0.75	0.11	0.19	-0.04	154.7K	5.2M	Transformer	E
BOWSR	0.42	1.96	0.30	0.71	0.72	0.69	0.12	0.17	0.15	133.4K	167.8K	BO-GNN	E
Voronoi RF	0.33	1.58	0.24	0.67	0.54	0.69	0.15	0.21	-0.33	154.7K	0.0	Fingerprint	E
Dummy	0.18	1.00	0.15	0.69	0.23	0.77	0.12	0.18	0.00				

S56.00005 Using first principles computations to understand and search for new transparent conducting materials

Geoffroy Hautier

Hole Mobility in CuI

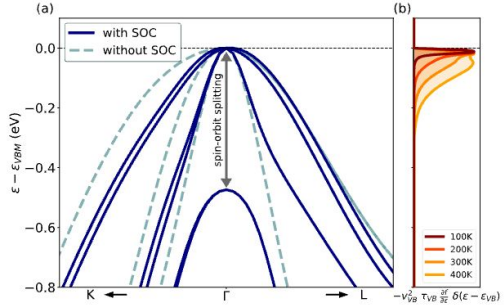

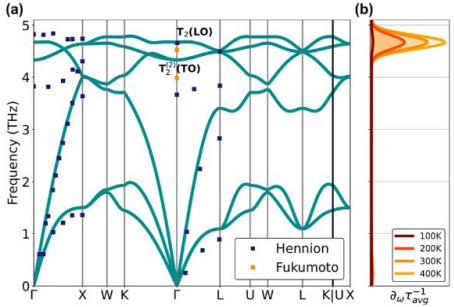

AMSET approach & analysis

- Polar optical phonons (POP)
- Acoustic deformation potential (ADP)
- Ionized impurities (IMP)
- Piezoelectric effects (PIE)

IBTE (Iterative Boltzmann Transport Equation) + Ionized impurities (IMP) performs the best.

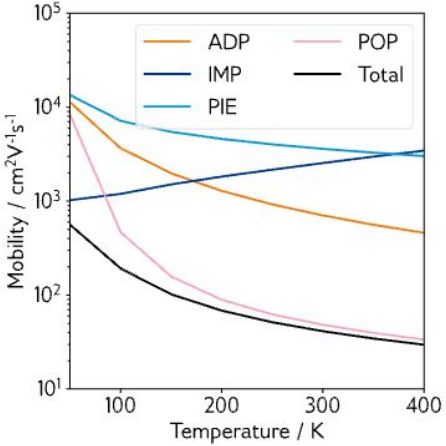

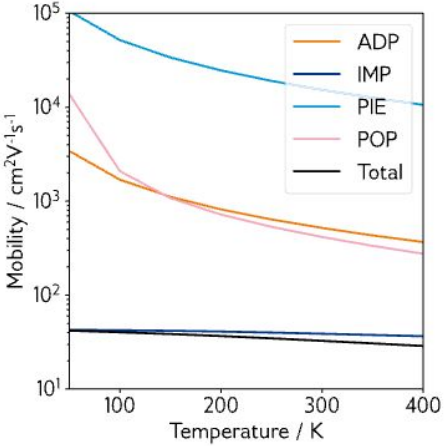

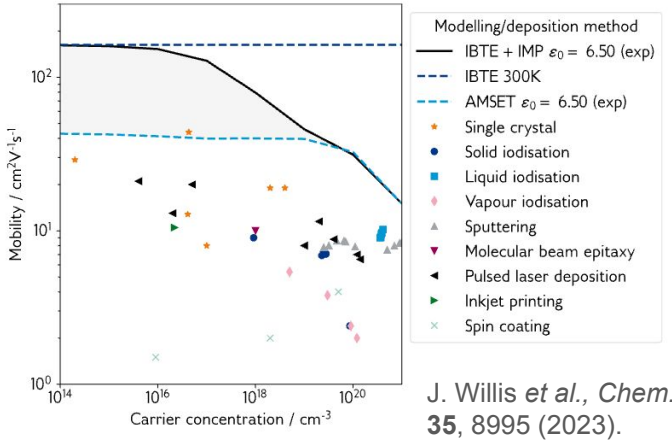

J. Willis *et al., Chem. Mater.* **35**, 8995 (2023).

W18.00001: Simulating structural phase transitions with simple models

Julia Dshemuchadse (Cornell University)

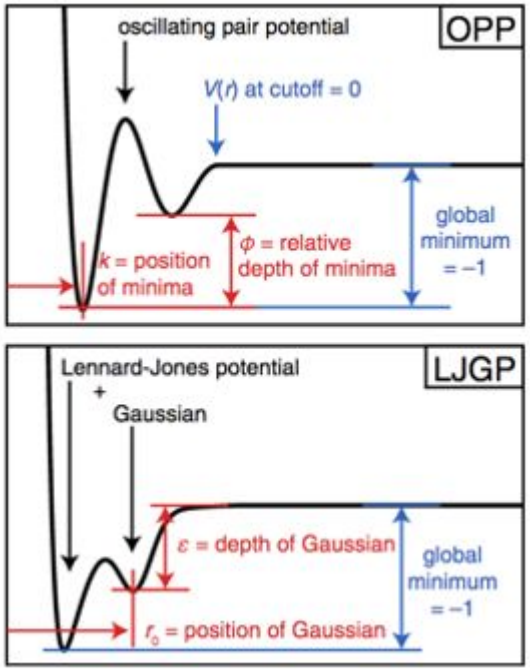

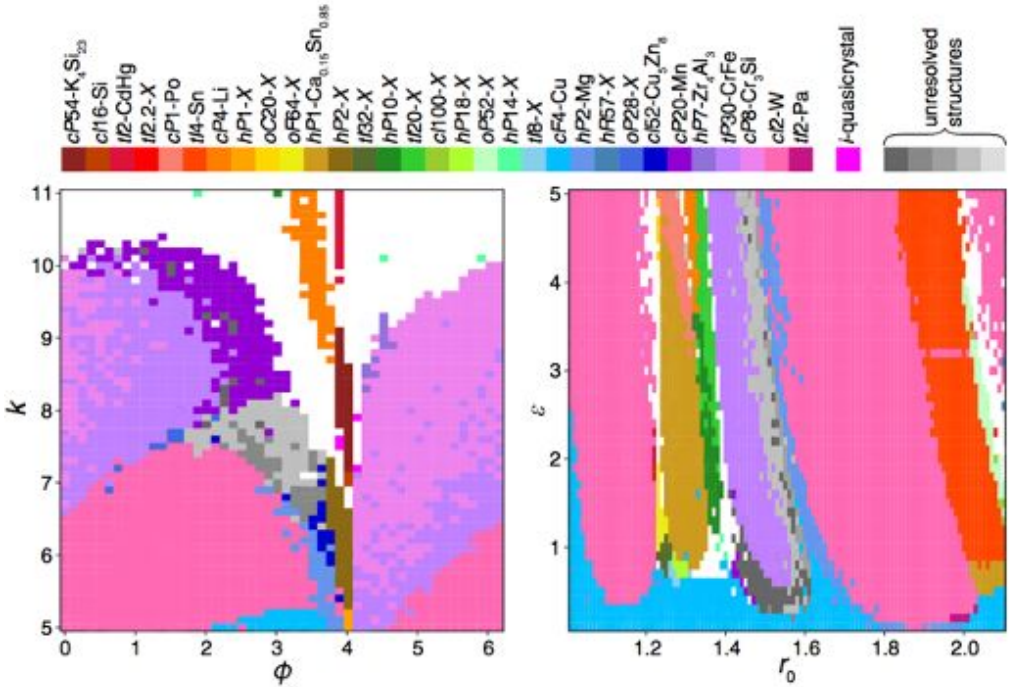

Reference: PNAS2021 Vol. 118 No. 21 e2024034118

W18.00001: Simulating structural phase transitions with simple models

Julia Dshemuchadse (Cornell University)

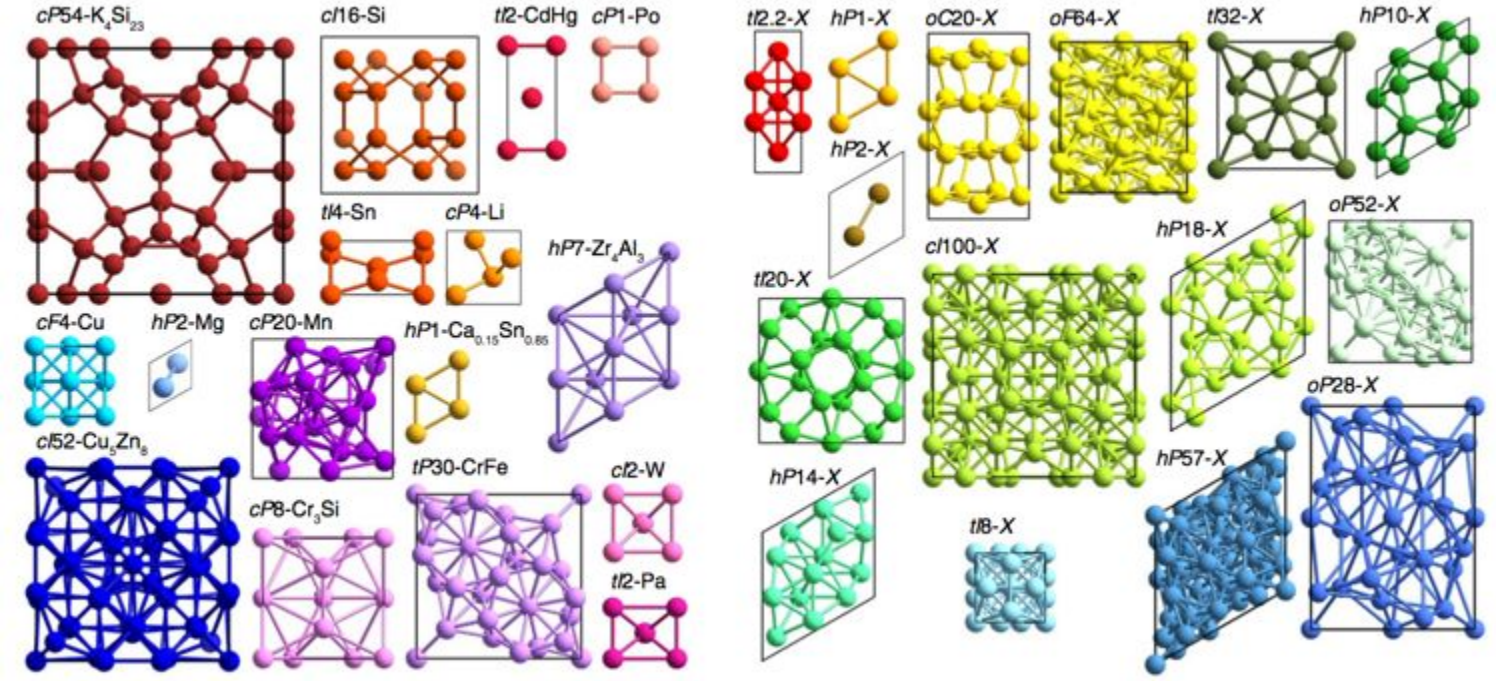

Reference: PNAS2021 Vol. 118 No. 21 e2024034118

W18.00001: Simulating structural phase transitions with simple models

Julia Dshemuchadse (Cornell University)

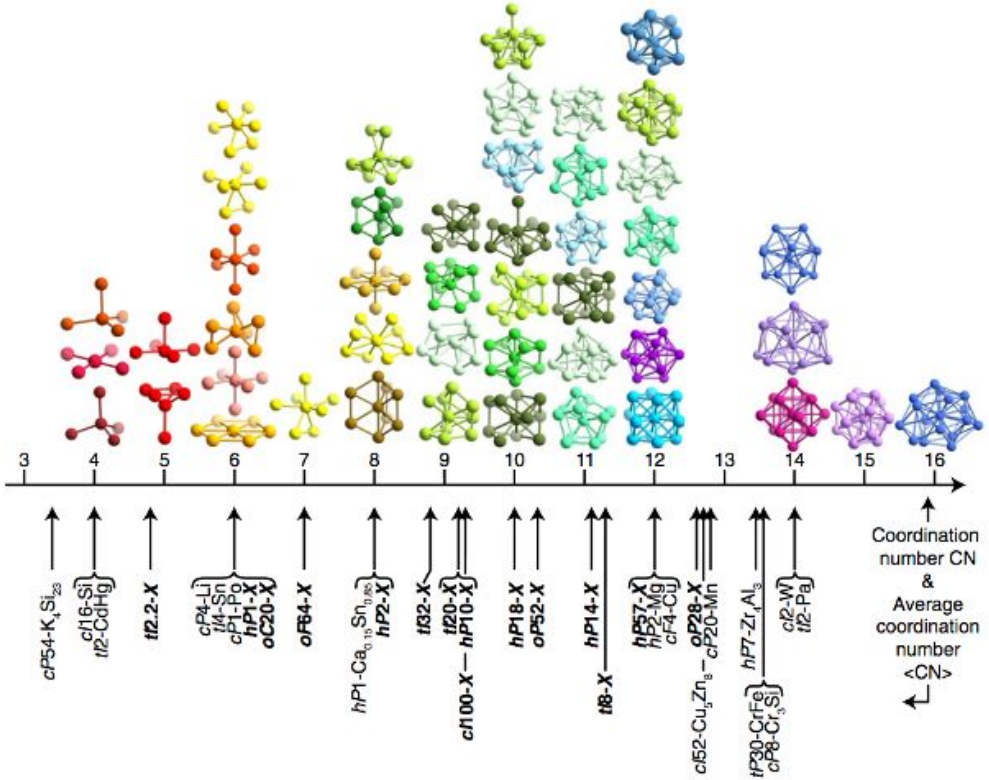

Reference: PNAS2021 Vol. 118 No. 21 e2024034118

Thank you for your contributions!